Nano Research

Open Access

Research Article

V_o-$AgFeO_{2-x}$ nanozymes treat infected wounds and promote wound healing

Hongrang Chen[1,§], Wenqi Wang[5,§], Yajuan Li[2,§], Lei Shu[5], Fan Ni[5], Huanchun Mei[4], Konglin Wu[4], Tingxuan Yan[4] ✉, Lei Shi[6] ✉, and Xianwen Wang[3,5] ✉

[1] *Department of Hepatobiliary Surgery, Department of General Surgery, the First Affiliated Hospital of Anhui Medical University, Hefei 230022, China*
[2] *Department of Clinical Laboratory, the First Affiliated Hospital of Anhui Medical University, Hefei 230022, China*
[3] *Department of Burns, The First Affiliated Hospital of Anhui Medical University, Hefei 230032, China*
[4] *Engineering Research Center of Biofilm Water Purification and Utilization Technology of Ministry of Education, Anhui University of Technology, Maanshan 243032, China*
[5] *School of Biomedical Engineering, Anhui Medical University, Hefei 230032, China*
[6] *Department of Ophthalmology, Anhui No 2 Provincial People's Hospital, Hefei 230041, China*
§ *Hongrang Chen, Wenqi Wang, and Yajuan Li contributed equally to this work.*

Cite this article: *Nano Research*, **2025**, *18*, 94907899. https://doi.org/10.26599/NR.2025.94907899

ABSTRACT: Effectively controlling bacterial infections and reducing oxidative stress and inflammatory reactions are important steps in wound healing. However, owing to the improper use of antibiotics and inadequate control of infections in recent years, the emergence of many broad-spectrum drug-resistant strains has exacerbated the threat of infected wounds to human health. Recent studies have shown that bimetallic nanozymes may become an effective means of treating drug-resistant bacterial infections because of their unique physical properties and excellent antibacterial properties. In this study, silver iron bimetallic nanozymes with multiple enzyme activities (peroxidase, glutathione peroxidase, and superoxide dismutase) were successfully synthesized for the treatment of skin wounds. Notably, the prepared V_o-$AgFeO_{2-x}$ exhibited different enzyme activities under different pH conditions. In acidic environments, V_o-$AgFeO_{2-x}$ can catalyze H_2O_2 to generate reactive oxygen species (ROS), deplete glutathione (GSH), and kill bacteria. In a neutral environment, V_o-$AgFeO_{2-x}$ can eliminate free radicals, control inflammatory reactions, and accelerate wound healing. *In vivo* experiments have shown that V_o-$AgFeO_{2-x}$ can promote the healing of infected wounds and has good biological safety. These findings suggest that it can be used as a safe and efficient antibacterial drug to achieve effective treatment of bacterial infection-induced wounds.

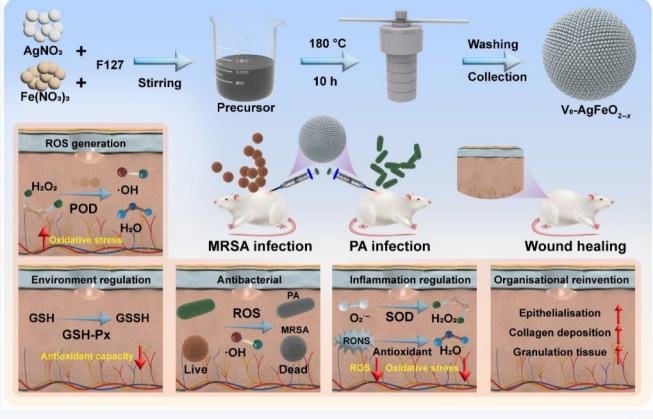

KEYWORDS: V_o-$AgFeO_{2-x}$, infected wounds, antibacterial therapy, wound healing, anti-inflammatory, pH response

1 Introduction

The treatment of wound bacterial infections is a significant challenge in contemporary medicine [1, 2]. Traditionally, antibiotics have been the primary method for treating wound bacterial infections, and their high efficacy in killing bacteria has made them widely used in clinical practice [3, 4]. However, with the continuous evolution of bacterial populations, some strains have developed resistance to antibiotics, diminishing their effectiveness [5, 6]. The emergence of antibiotic-resistant bacteria has resulted in the reduced efficacy of traditional antibiotics, presenting considerable challenges, especially when infections are difficult to control and treatment options are limited [7–9]. Furthermore, wound bacterial infections are often associated with inflammatory responses and

Received: July 1, 2025; **Revised:** August 5, 2025
Accepted: August 6, 2025

✉Address correspondence to Xianwen Wang, xianwenwang@ahmu.edu.cn; Lei Shi, shileidr@outlook.com; Tingxuan Yan, chinaytx@ahut.edu.cn

tissue damage. These inflammatory responses not only exacerbate the pathological condition at the infection site but also may lead to systemic complications, increasing the difficulty of recovery [10, 11]. The repair process of tissue damage is further hindered by persistent inflammation, resulting in prolonged recovery periods [9, 12]. The complexity of inflammation and damage necessitates that treatment not only targets bacterial infection but also addresses inflammatory issues, increasing the demand for existing treatment strategies [13–15]. Moreover, the misuse or overuse of antibiotics undoubtedly exacerbates the emergence of resistant bacteria, making clinical treatment more challenging [16, 17]. The overuse of antibiotics leads to the waste of resources and medications and, in the long term, increases public health risks [18]. The global rise in antibiotic-resistant bacteria poses a serious threat to public health [19]. To address these challenges, researchers are actively exploring new therapeutic strategies. Metal-based nanomaterials with enzymatic activities, such as oxidase (OXD), peroxidase (POD), and superoxide dismutase (SOD), have shown significant potential in the treatment of wound bacterial infections [20–22]. These nanomaterials can specifically target and kill resistant bacteria, reduce inflammation, and accelerate tissue repair, suggesting new directions for clinical treatment [23–25].

Ag metal nanocatalysts are highly valuable in the nanotechnology and biomedical fields because of their exceptional catalytic performance, pronounced antimicrobial effects, good biocompatibility, and broad application potential [26–28]. Notably, the introduction of oxygen vacancies in metal nanocatalysts can significantly enhance their performance characteristics [29, 30]. Oxygen vacancies notably increase the density of active sites on the catalyst surface, thereby enhancing the overall catalytic efficiency by improving the contact between reactants and the catalyst [31, 32]. This is crucial for increasing the catalytic ability of metal nanocatalysts in redox reactions [33–35]. Furthermore, oxygen vacancies can improve electron transfer properties, accelerate reaction rates, and enhance catalytic activity, especially in complex environments [36–38]. Additionally, oxygen vacancies contribute to the stability and biocompatibility of nanocatalysts, maintaining their activity in complex biological environments while reducing potential toxicity [39, 40]. The primary goal of introducing oxygen vacancies is to address the stability challenges faced by silver in practical applications and enhance its persistence in wound environments [41, 42]. In bimetallic nanomaterials, the role of iron is also critical. Iron significantly increases the catalytic activity by facilitating electron transfer processes, thereby improving the overall catalytic efficiency [43, 44]. The introduction of iron also enhances the stability of the catalyst, ensuring sustained activity in complex biological settings [45, 46]. Furthermore, iron can modulate catalytic performance, affecting reaction pathways and selectivity, which optimizes the overall catalytic effect [47–49]. Iron itself also possesses antimicrobial properties, which, when combined with silver or other metals, further strengthen its antimicrobial efficacy [50]. Therefore, iron plays a pivotal role in bimetallic nanomaterials, supporting improved overall performance, enhanced antimicrobial effects, and accelerated wound healing [51, 52].

In this study, an improved solvothermal method was employed to synthesize $AgFeO_2$ materials by incorporating the F127 polymer surfactant during the preparation process, which enhanced the dispersion of the nanoparticles (NPs) and successfully produced bimetallic nanocatalysts with oxygen defects (V_o-$AgFeO_{2-x}$). The V_o-$AgFeO_{2-x}$ nanocatalysts exhibit various enzyme activities, including efficient antibacterial effects, effective inflammation control, and promotion of wound healing (Scheme 1). A detailed characterization of the oxygen vacancies in V_o-$AgFeO_{2-x}$ was conducted, an aspect not previously reported. The experimental results demonstrated that V_o-$AgFeO_{2-x}$ has POD-like catalytic activity under acidic conditions, effectively generating reactive oxygen species to kill bacteria. Under neutral conditions, it displays SOD-like activity, which helps eliminate free radicals and accelerates wound healing. *In vivo* experiments further confirmed the outstanding antibacterial efficacy of V_o-$AgFeO_{2-x}$. These nanoparticles not only overcome the limitations of single silver and iron nanocatalysts but also significantly increase the stability and broaden the antibacterial spectrum. Notably, the application of V_o-$AgFeO_{2-x}$ in this study differs from that in previous reports in that it focused on the multifaceted treatment of bacterium-infected wounds. Additionally, V_o-$AgFeO_{2-x}$ has excellent biocompatibility with negligible toxicity, making it a safe and effective antimicrobial agent. This work highlights the multienzyme activities of V_o-$AgFeO_{2-x}$ and its tremendous potential in combating bacterial infections and promoting wound healing.

2 Experimental section

2.1 Chemical reagents

$AgNO_3$, $Fe(NO_3)_3{\cdot}9H_2O$, and potassium hydroxide (KOH) were purchased from Sinopharm Group Co., Ltd. Polyethylene-polypropylene glycol (F127) was purchased from Shanghai Aladdin Biochemical Technology Co., Ltd. The water used was deionized water. All chemicals were used as received without further purification.

2.2 Preparation of oxygen-vacancy $AgFeO_{2-x}$ nanozymes (V_o-$AgFeO_{2-x}$ NPs)

The V_o-$AgFeO_{2-x}$ NPs were prepared via a modified solvothermal method [53]. The typical preparation process was as follows: 1.5 mmol of $AgNO_3$, 1.5 mmol of $Fe(NO_3)_3{\cdot}9H_2O$, and 0.1 g of F127 were dissolved in 25 mL of deionized water under stirring for 20 min. Then, 0.45 g of KOH was added, and the mixture was stirred for another 20 min. Finally, the suspension was transferred to a 50 mL Teflon-lined reactor and placed in an oven to react at 180 °C for 10 h. When the reaction finished, the mixture was cooled naturally to room temperature. The precipitate was centrifuged and washed with deionized water and ethanol, and then, the V_o-$AgFeO_{2-x}$ NPs were obtained.

2.3 Materials characterization

X-ray powder diffraction (XRD, Bruker D8 advance) was used to characterize the product purity and phase structure. The morphologies and elemental mapping were characterized via high-resolution field emission transmission electron microscopy (TEM, Thermo Fisher, Talos F200S). The atomic phases of the samples were characterized via aberration-corrected scanning transmission electron microscopy (AC-STEM). X-ray photoelectron spectroscopy (XPS, Thermo Fisher, ESCALAB Xi+) was used to characterize the elemental valence of the samples. Oxygen vacancies were detected by electron paramagnetic resonance (EPR, EMX-10/12, Bruker). The laser confocal microimaging system (CSIM-130) was obtained from Beijing Century Sunny Technology Co. Multi-function

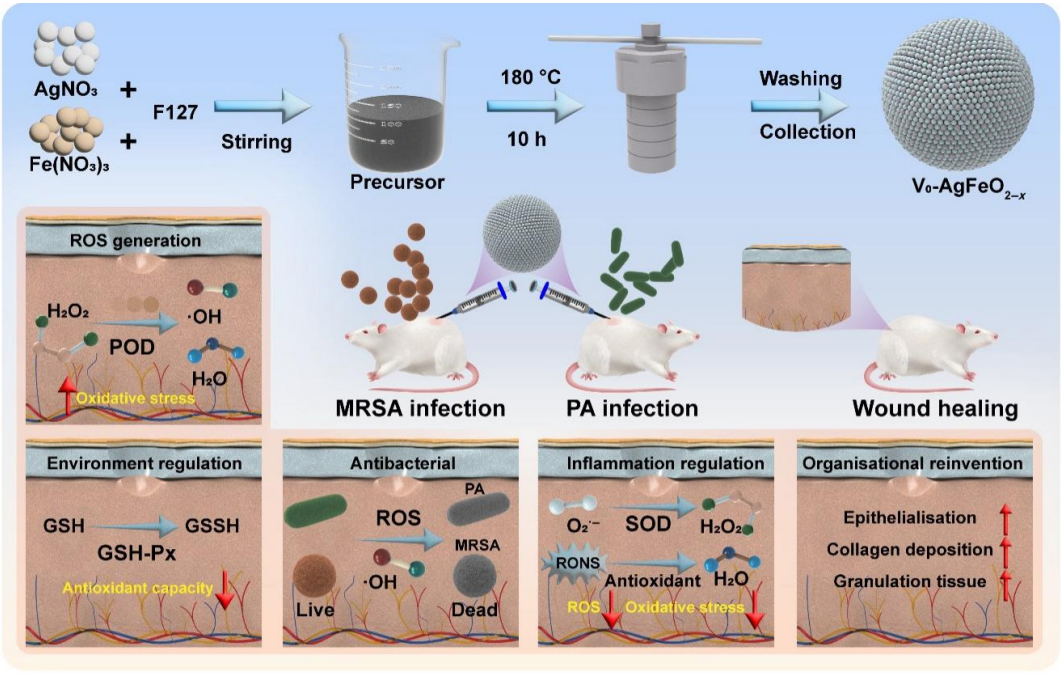

Scheme 1 Scheme of the mechanism by which multiple enzymatic activities of V_o-$AgFeO_{2-x}$ promote wound healing.

enzyme labeller (SpectraMax iD3) from Meigu Molecular Instruments (Shanghai) Co.

2.4 *In vitro* antibacterial experiments

Both gram (−) bacteria (PA) and gram (+) bacteria (Mu50) were used as infecting strains. Glycerol-stored strains were removed from −80 °C for inoculation into Luria–Bertani media. The samples were incubated for 12 h at 37 °C. The bacterial concentration was measured via a UV spectrophotometer at an absorbance value of 600 nm. In a typical antibacterial assay, *PA* and *MRSA* were divided into the following four groups: (I) control (bacteria + PBS), (II) bacteria + H_2O_2 (0.08 mM), (III) bacteria + V_o-$AgFeO_{2-x}$ NPs, and (IV) bacteria + V_o-$AgFeO_{2-x}$ + H_2O_2 (0.08 mM). The V_o-$AgFeO_{2-x}$ concentration gradient was set at 0, 0.01, 0.1, 0.2, 0.5, and 1 mg/mL. H_2O_2 (80 μM) was used, and the bacterial concentration was 1×10^6 CFU/mL. Thirty microlitres of the bacteria were incubated in the oven for 3 h, and 30 μL of the bacteria was spread uniformly on LB. The colonies were counted via incubation for 15 h at 37 °C via ImageJ. The incubation was repeated three times.

2.5 Scanning electron microscope (SEM) measurements

Bacteria were treated for 3 h according to the four subgroups: (I) control (bacteria + PBS), (II) bacteria + H_2O_2 (0.08 mM), (III) bacteria + V_o-$AgFeO_{2-x}$ NPs, and (IV) bacteria + V_o-$AgFeO_{2-x}$ + H_2O_2 (0.08 mM). The samples were subsequently centrifuged at 4000 rpm for 5 min, after which the supernatant was removed. One milliliter of 2.5% glutaraldehyde was added, and the mixture was placed in a refrigerator at 4 °C for 12 h for fixation. A gradient wash using 10%, 30%, 50%, 70%, and 90% ethanol was subsequently performed for dehydration. Finally, 20 μL bacterial samples were placed dropwise on a silicon wafer for SEM.

2.6 Live/dead fluorescence staining

N01 (green) and propidium iodide (PI) (red) were used for live/dead fluorescence staining. Four subgroups were treated as follows: (I) control (bacteria + PBS), (II) bacteria + H_2O_2 (0.08 mM), (III) bacteria + V_o-$AgFeO_{2-x}$ NPs, and (IV) bacteria + V_o-$AgFeO_{2-x}$ + H_2O_2 (0.08 mM). Live and dead bacteria were stained with N01 (live) and PI (dead). Fluorescent photographs were taken via laser confocal microscopy.

2.7 *In vivo* antibacterial activity and wound healing

All animal procedures were performed in compliance with the guidelines of the Institutional Animal Care and Use Committee of the Department of Anhui Medical University. The mice were divided randomly into eight groups of five groups: (a) *MRSA* + control (PBS); (b) *MRSA* + H_2O_2; (c) *MRSA* + V_o-$AgFeO_{2-x}$ NPs; (d) *MRSA* + V_o-$AgFeO_{2-x}$ NPs + H_2O_2; (e) *PA* + control (PBS); (f) *PA* + H_2O_2; (g) *PA* + V_o-$AgFeO_{2-x}$ NPs; and (h) *PA* + V_o-$AgFeO_{2-x}$ NPs + H_2O_2. The concentration of V_o-$AgFeO_{2-x}$ NPs used was 1 mg/mL and the concentration of H_2O_2 used was 0.08 mM. The right sides of the mice were shaved, and the mice were then anesthetized with pentobarbital sodium. A skin wound of ~ 40 mm^2 was created by nicking with a sterile scalpel. Then, the bacterial suspension (50 μL, 1×10^9 CFU/mL) was gradually inoculated onto the wound, and the moisture was allowed to evaporate naturally. After 12 h, the mouse infected wound model was constructed. Then, 50 μL of V_o-$AgFeO_{2-x}$ NPs (1 mg/mL) and 50 μL of H_2O_2 (100 μM) were added directly dropwise to the infected wounds in the V_o-$AgFeO_{2-x}$ NP + H_2O_2 treatment group. The other three groups were subjected to the same procedure. The wound healing images were recorded via a video camera, and the wound area was calculated at 3, 5, 7, 9, and 11 days via ImageJ. The percentage of unhealed area was calculated as $[A_{(3,\,5,\,7,\,9,\,11)}/A_0] \times 100\%$. A_0 and $A_{(3,\,5,\,7,\,9,\,11)}$ represent the unhealed areas on day 0 and days 3, 5, 7, 9 and 11, respectively. The body weights of the mice were recorded daily. On day 11, mouse skin tissues were collected for caseological analysis. Wounds were subjected to hematoxylin and eosin (H&E) staining and Masson's trichrome. Mouse organs heart, liver, spleen, lung, and kidney were stained with H&E.

3 Results and discussion

3.1 Synthesis and characterization of the V_o-$AgFeO_{2-x}$ NPs

Here, V_o-$AgFeO_{2-x}$ NPs were successfully prepared via a solvothermal method. The purity and phase structure of the obtained samples were examined via XRD, and the results revealed that the obtained sample had a hexagonal-phase V_o-$AgFeO_{2-x}$ (JCPDS No. 21--1081) structure [53]. The morphologies and sizes of the obtained V_o-$AgFeO_{2-x}$ products were characterized via TEM. As shown in Fig. 1(a), V_o-$AgFeO_{2-x}$ particles with sizes ranging from approximately 100–200 nm were observed. The high-resolution TEM (HRTEM) image (Fig. 1(b)) shows that the clear lattice spacing is 0.26 nm, which can be attributed to the (101) crystal plane of the hexagonal phase V_o-$AgFeO_{2-x}$ (JCPDS No. 21--1081). The selected area electron diffraction (SAED) pattern (Fig. 1(c)) shows that the as-prepared V_o-$AgFeO_{2-x}$ NPs have a single-crystal structure, and the three typical diffraction points can be indexed to the (102), (009), and (104) crystal planes of hexagonal-phase V_o-$AgFeO_{2-x}$ (JCPDS No. 21--1081). High-angle circular dark field scanning TEM (HAADF-STEM, Fig. 1(d)) and corresponding energy-dispersive spectroscopy (EDS) elemental mapping images (Figs. 1(e)–1(h)) of the V_o-$AgFeO_{2-x}$ NPs indicate that Ag, Fe, and O are evenly distributed on the NPs. Aberration-corrected-STEM (AC-STEM) images (Fig. 1(i)) show that the interior of the NPs is highly crystalline and that the surface layer of approximately 1 nm on the NPs is amorphous, which proves the existence of a surface defect layer. Furthermore, we enlarged area A in Fig. 1(i), and the high-resolution AC-STEM image (Fig. 1(j)) shows that its regular atomic arrangement also indicates its high crystallinity. The intensity profile image (Fig. 1(k)) along area B in Fig. 1(j) shows that the lattice spacing is approximately 0.2 nm, which can be indexed to the (009) of the hexagonal phase V_o-$AgFeO_{2-x}$ (JCPDS No. 21--1081).

XPS was further used to determine the presence of Ag, Fe, and O

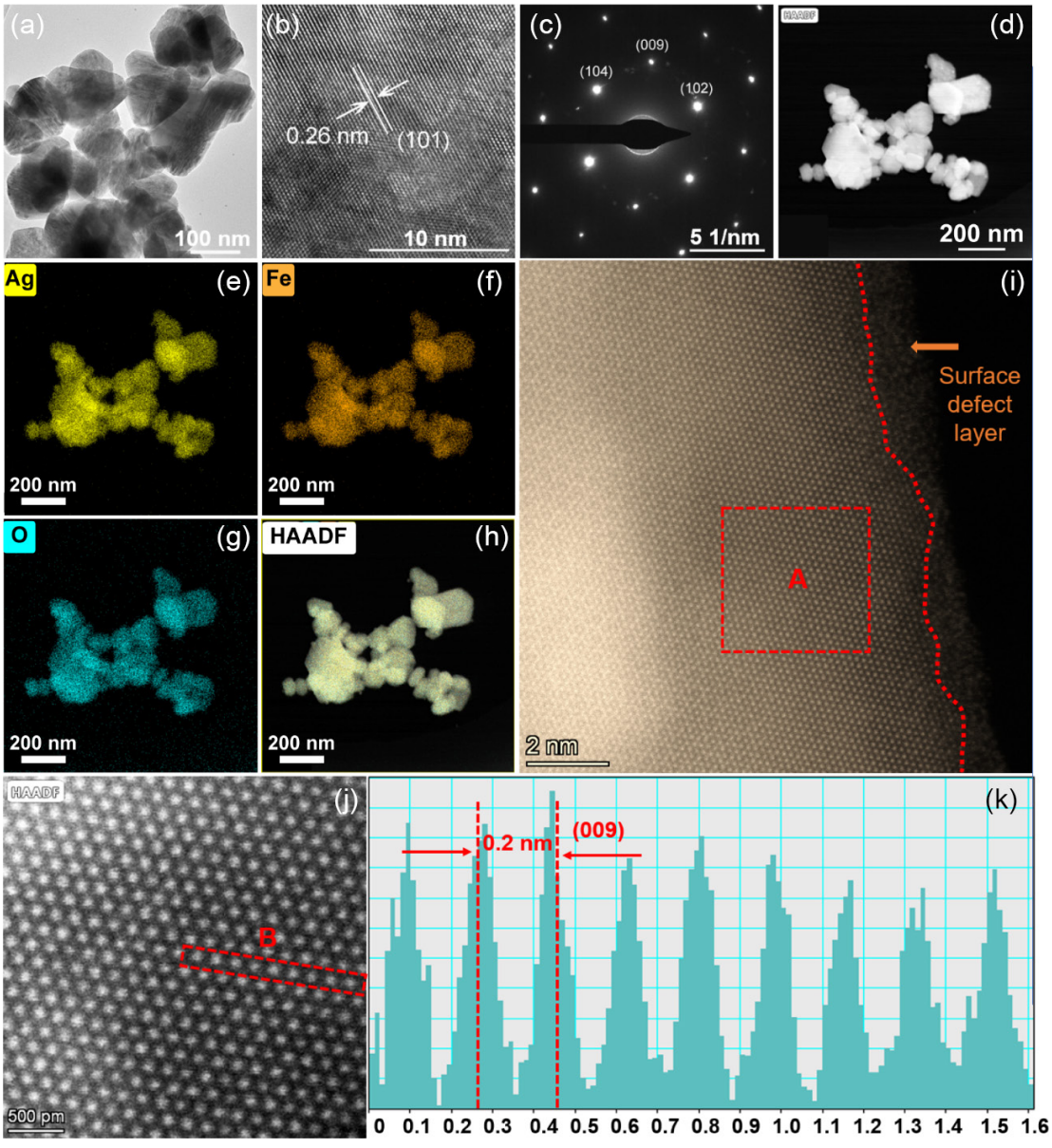

Figure 1 Characterization of the V_o-$AgFeO_{2-x}$ NPs. (a) TEM, (b) HRTEM, (c) SAED, (d) HAADF-STEM, and ((e)–(h)) corresponding EDS elemental mapping images of the V_o-$AgFeO_{2-x}$ NPs. (i) AC-STEM image and (j) local magnified AC-STEM image from (i) (area A). (k) Intensity profile along area B in (j).

in the V_o-$AgFeO_{2-x}$ NPs. The survey XPS spectrum revealed that Ag, Fe, and O were present. The typical Ag 3d XPS spectrum (Fig. 2(a)) shows that the binding energies at 374 and 368 eV are indexed to Ag $3d_{3/2}$ and Ag $3d_{5/2}$, respectively. The Fe 2p XPS spectrum (Fig. 2(b)) shows that the binding energies at 724.6 and 711.1 eV are attributed to Fe $2p_{1/2}$ and Fe $2p_{3/2}$, respectively, and those at 732.2 and 719 eV are attributed to satellite (Sat.) peaks. Excitingly, we detected the absorption of H_2O in the O 1 s XPS spectrum (Fig. 2(c)), indicating the presence of V_o in the V_o-$AgFeO_{2-x}$ NPs. To further confirm the existence of V_o, the V_o-$AgFeO_{2-x}$ NPs were characterized by EPR spectroscopy (Fig. 2(d)). According to calculations, the g value of the V_o-$AgFeO_{2-x}$ NPs is 2.007, which proves the existence of V_o in the V_o-$AgFeO_{2-x}$ NPs. The successful preparation of oxygen vacancy materials has laid a foundation for their application and development in biomedicine.

3.2 Multiple enzyme activities of the V_o-$AgFeO_{2-x}$ NPs

Iron-based nanozymes mimic many oxidoreductases with multiple enzyme activities and have been widely studied for antibacterial treatment and wound healing (Fig. 3(a)). However, silver iron bimetallic nanomaterials have not been reported to use multiple enzyme activities to kill bacteria and promote wound healing. Phenylenediamine (OPD) is easily oxidized by a variety of oxidants to produce the yellow fluorescent substance 2,3-diaminophenazine (ox-OPD), which has a characteristic peak at 416 nm. Owing to its high sensitivity and strong anti-interference ability, we used OPD as a chromogenic substrate to evaluate the POD enzyme activity of V_o-$AgFeO_{2-x}$. Compared with those of the other groups, the reaction solutions containing V_o-$AgFeO_{2-x}$, H_2O_2, and OPD presented a deeper color and a greater absorbance peak at 416 nm. These findings indicate that V_o-$AgFeO_{2-x}$ has good POD-like activity (Fig. 3(b)). The POD-like activity of V_o-$AgFeO_{2-x}$ was closely related to the concentration of H_2O_2 and the material, and its activity significantly increased with increasing H_2O_2 concentrations or material concentrations (Figs. 3(c) and 3(d)). EPR spectroscopy was used to detect the free radicals generated in the reaction system. The results showed that the reaction of V_o-$AgFeO_{2-x}$ with H_2O_2 could produce superoxide anions and hydroxyl radicals (Fig. 3(e)). Controlling the inflammatory reaction at the wound site is one of the key steps in promoting wound healing. To evaluate the anti-inflammatory activity of V_o-$AgFeO_{2-x}$, we performed ABTS and DPPH scavenging experiments to verify the antioxidant capacity of V_o-$AgFeO_{2-x}$. Researchers usually use 2,2′ -azino-bis(3-ethylbenzothiazoline-6-sulfonic acid) (ABTS) and 2,2-diphenyl-1-picrylhydrazyl (DPPH) to evaluate the ability of nanomaterials to scavenge reactive nitrogen species (RNS). The absorbance of the ABTS radical solution treated with different concentrations of V_o-$AgFeO_{2-x}$ attenuated the most at the 734 nm characteristic peak, and the color change was the most obvious (Fig. 3(f)). Its clearance was then determined by the change in absorbance at 734 nm (Fig. 3(g)). During the reaction with the DPPH radical solution, the characteristic peak at 517 nm also changed significantly (Fig. 3(h)), and the clearance rate was determined accordingly (Fig. 3(i)). The changes in the ABTS and DPPH results indicated that V_o-$AgFeO_{2-x}$ had the ability to scavenge RNS. Glutathione (GSH) is an important member of the cellular antioxidant system. Many studies have shown that GSH consumption can improve the therapeutic effect of ROS-based therapy [45, 46]. 5,5'-Dithiobis (2-nitrobenzoic acid) (DTNB) was used as a probe to test the GSH depletion ability of V_o-$AgFeO_{2-x}$. After the reaction between GSH and V_o-$AgFeO_{2-x}$, the depletion rate of GSH was determined on the basis of the change in absorbance at its characteristic peak (Fig. 3(j)). Following incubation with V_o-$AgFeO_{2-x}$ for 6 h at a concentration of 50 μg/mL, GSH was entirely consumed (Fig. 3(k)), suggesting that

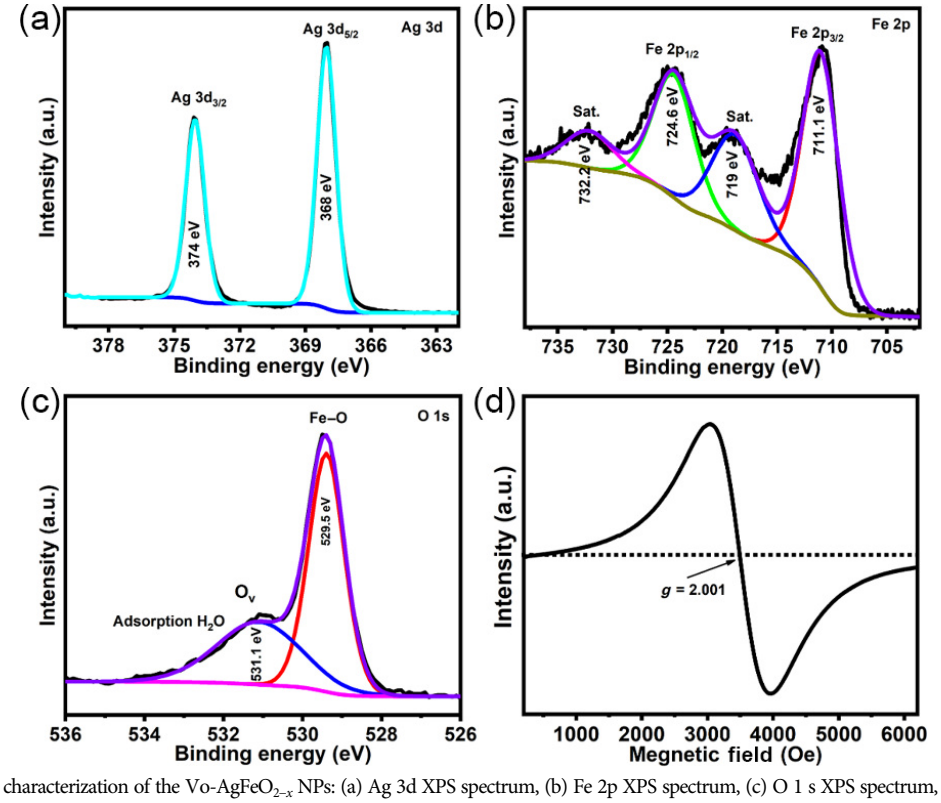

Figure 2 XPS and EPR characterization of the Vo-$AgFeO_{2-x}$ NPs: (a) Ag 3d XPS spectrum, (b) Fe 2p XPS spectrum, (c) O 1 s XPS spectrum, and (d) EPR spectrum of the V_o-$AgFeO_{2-x}$ NPs.

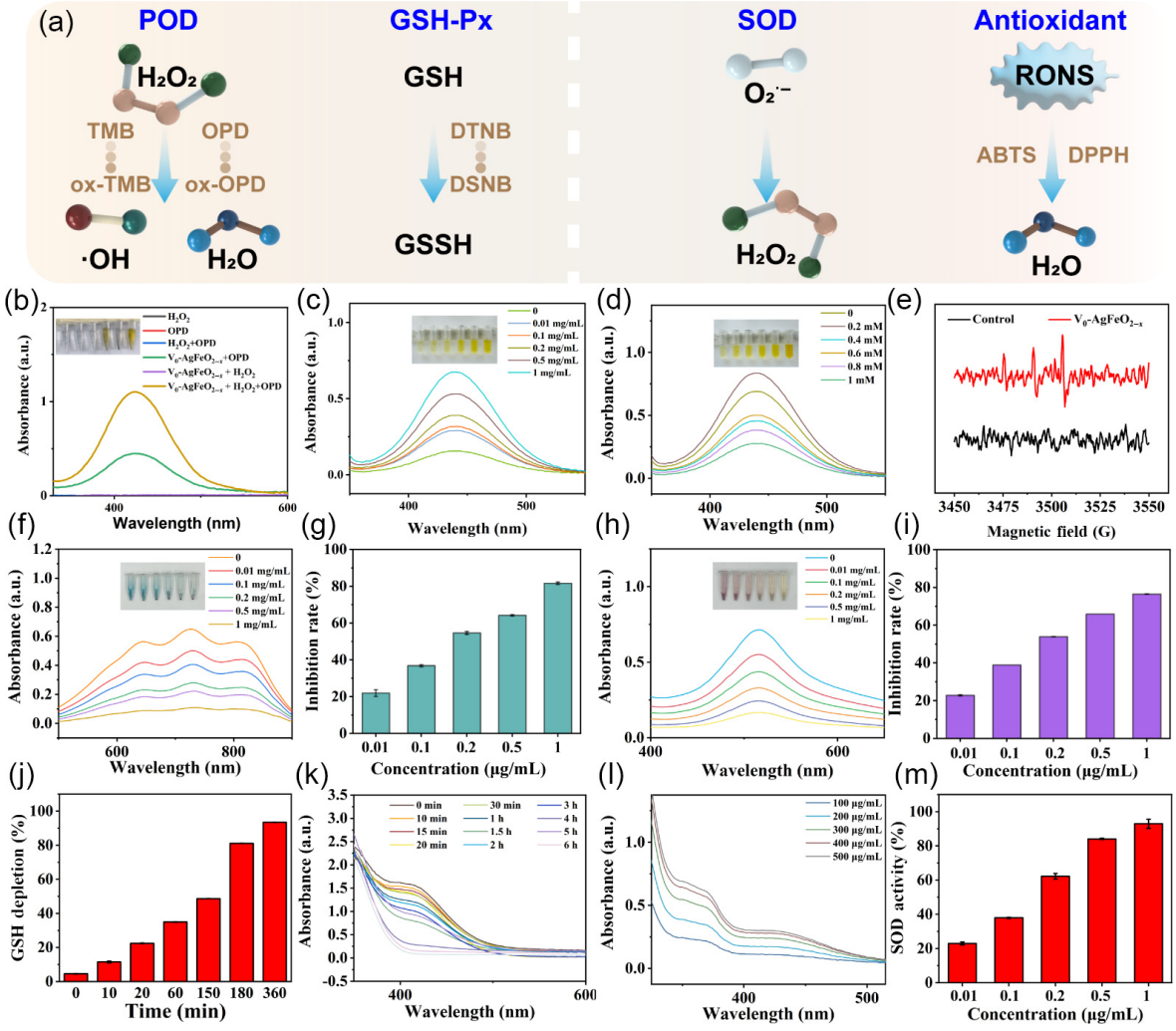

Figure 3 Multienzyme activity of V_o-$AgFeO_{2-x}$ NPs. (a) Diagram of the mechanism underlying the activity of the enzyme. (b) UV–vis spectra of solutions containing OPD alone, H_2O_2, OPD + H_2O_2, V_o-$AgFeO_{2-x}$ + OPD, V_o-$AgFeO_{2-x}$ + H_2O_2, and V_o-$AgFeO_{2-x}$ + OPD + H_2O_2 after a 20 min reaction. (c) POD-like activity at different V_o-$AgFeO_{2-x}$ concentrations determined via the OPD probe. (d) POD-like activity at different H_2O_2 concentrations determined via the OPD probe. (e) EPR detection of free radical generation. (f) ROS scavenging activity and (g) scavenging rate of V_o-$AgFeO_{2-x}$ at different concentrations measured using the ABTS probe. (h) ROS scavenging activity and (i) scavenging rate of V_o-$AgFeO_{2-x}$ at different concentrations measured using the DPPH probe. (j) GSH consumption rates of the V_o-$AgFeO_{2-x}$ NPs at different times. (k) Time-dependent GSH scavenging activity of V_o-$AgFeO_{2-x}$ NPs at a concentration of 50 μg/mL. (l) POD-like activity absorbance curves for different concentrations of V_o-$AgFeO_{2-x}$ NPs. (m) SOD-like activity of the V_o-$AgFeO_{2-x}$ NPs determined at different concentrations via a WST-8 total SOD detection kit.

Cu-GA had good GSH-Px-like nanozyme activity. In accordance with the principle of H_2O_2 catalysis by POD, the POD-like activity of V_o-$AgFeO_{2-x}$ was determined by measuring the change in absorbance at 420 nm (Fig. 3(l)). The SOD activity of V_o-$AgFeO_{2-x}$ was determined via the WST-8 method (Fig. 3(m)), and the results revealed that V_o-$AgFeO_{2-x}$ had good SOD-like activity. In addition, POD-like and GSH-Px-like enzymes with peroxidase activity maintained higher catalytic activity under acidic conditions (pH 5.0) than at pH 7.0. This result is consistent with the acidic microenvironment in bacterium-infected wounds, which facilitates the efficient production of ROS by enzymes to kill bacteria (Figs. S1(a) and S1(b) in the Electronic Supplementary Material (ESM)). However, SOD-like activity had optimal catalytic activity at pH 7.0 and reduced catalytic activity at slightly acidic (pH 6.0) and slightly alkaline (pH 8.0) pH values, possibly because the changes in acidic and alkaline environments are related mainly to the structure of the enzyme and the nature of the active center. This result favors a reduction in the inflammatory response after bacteria are cleared (Fig. S1(c) in the ESM). The long-term stability of nanomedicines is important for their medical applications. To verify the long-term stability of V_o-$AgFeO_{2-x}$, POD-like, GSH-Px-like, and SOD-like activities were tested using V_o-$AgFeO_{2-x}$ stored for 0–100 days. The enzymatic activities of V_o-$AgFeO_{2-x}$ remained stable after 100 days of storage (Fig. S2 in the ESM).

3.3 *In vitro* antibacterial activity of the V_o-$AgFeO_{2-x}$ NPs

To evaluate antibacterial activity, we initially conducted *in vitro* experiments to assess the antimicrobial effects of V_o-$AgFeO_{2-x}$ NPs against various bacteria. Given the significant antibacterial properties of silver, we chose two representative bacterial strains: methicillin-resistant *Staphylococcus aureus* (*MRSA*) and *Pseudomonas aeruginosa* (*PA*). Different concentrations of V_o-$AgFeO_{2-x}$ NPs were applied to agar plates to observe their effects on bacterial growth. The results indicated that at a concentration of 0 μg/mL V_o-$AgFeO_{2-x}$ NPs, the agar plates were covered with numerous bacterial colonies, suggesting that there was no

significant antibacterial effect at this concentration. However, as the concentration of V_o-$AgFeO_{2-x}$ NPs increased, the number of bacterial colonies for both types of bacteria significantly decreased. This observation suggested that the V_o-$AgFeO_{2-x}$ NPs exhibited strong antibacterial activity (Figs. 4(a) and 4(b)). This superior antimicrobial capacity is closely related to the possible presence of silver nanocatalysts and silver ions. Previous studies have indicated that silver nanoparticles (AgNPs) exert their antibacterial effects by altering cell membrane permeability, inhibiting intracellular enzyme activity, and blocking DNA synthesis and replication. Additionally, silver ions, as heavy metal ions, can work synergistically with AgNPs to induce oxidative stress, further enhancing their antibacterial efficacy. To further validate the antibacterial performance of the V_o-$AgFeO_{2-x}$ NPs, comparative experiments were carried out with the following control groups: PBS control, H_2O_2 (0.08 mM), V_o-$AgFeO_{2-x}$ NPs, and V_o-$AgFeO_{2-x}$ + H_2O_2 (0.08 mM). Compared with the PBS control group, the H_2O_2 group presented weaker antibacterial effects, whereas the V_o-$AgFeO_{2-x}$ NP group presented significantly greater antibacterial activity than the H_2O_2 group. This result may be attributed to the concentration of H_2O_2, as high concentrations of H_2O_2 can cause cellular damage, limiting its antibacterial effects. H_2O_2, a commonly used disinfectant and antimicrobial agent, exerts its antibacterial mechanism primarily through the generation of hydroxyl radicals (·OH), which can damage major biomolecules in cells, including DNA, proteins, and phospholipids, ultimately leading to bacterial death. Given that ·OH is a highly toxic ROS with broad-spectrum antimicrobial activity, the synergistic effect of V_o-$AgFeO_{2-x}$ NPs

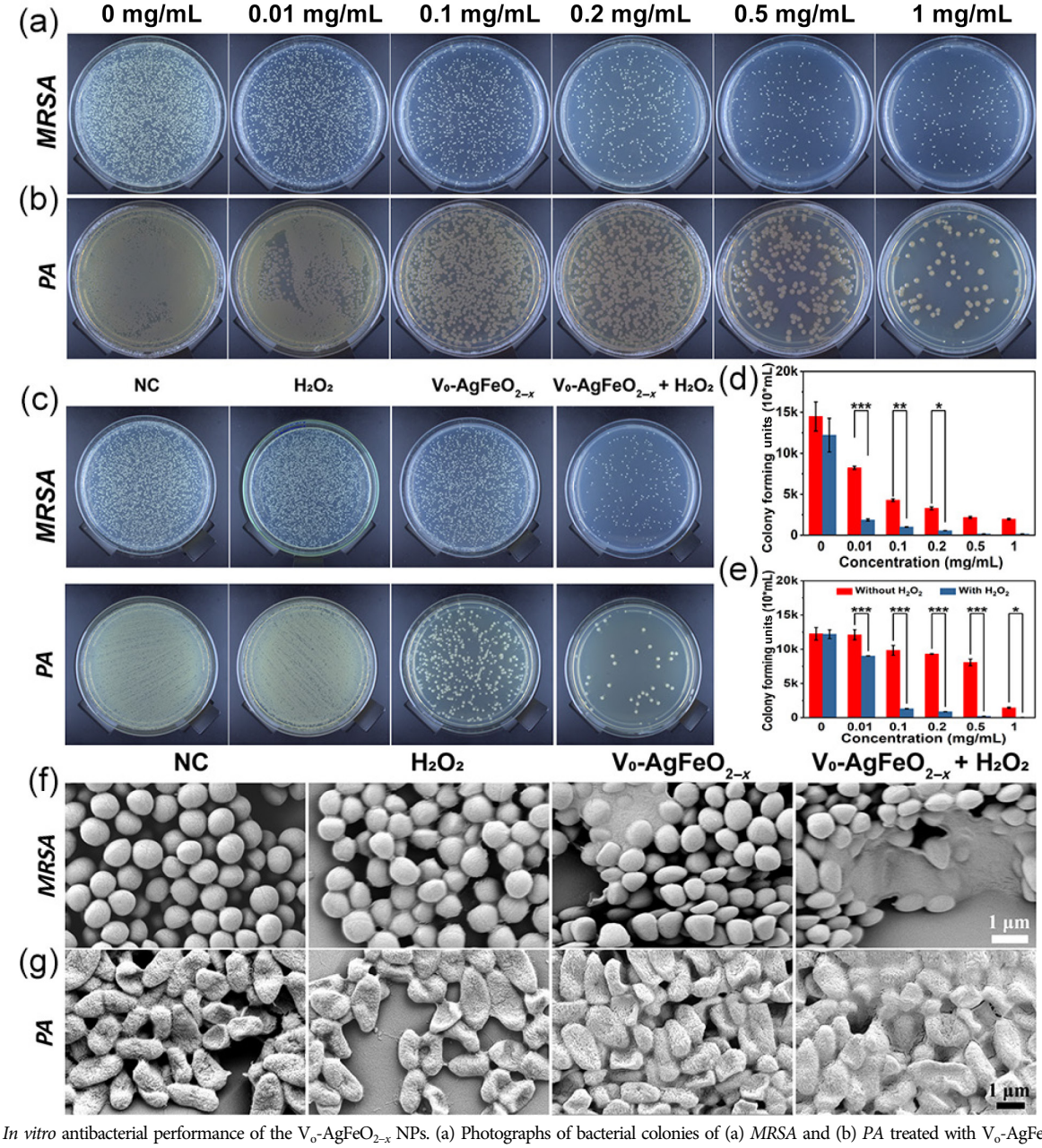

Figure 4 *In vitro* antibacterial performance of the V_o-$AgFeO_{2-x}$ NPs. (a) Photographs of bacterial colonies of (a) *MRSA* and (b) *PA* treated with V_o-$AgFeO_{2-x}$ NPs at various concentrations. (c) Photographs of bacterial colonies and colony-forming units of *MRSA* (d) and *PA* (e) after different treatments. (f) SEM images of *MRSA* after various treatments. (g) SEM images of *PA* after various treatments. Statistical analysis was performed via Student's two-tailed *t* test (***$P < 0.001$, **$P < 0.01$, and *$P < 0.05$).

with H_2O_2 was further explored. V_o-$AgFeO_{2-x}$ NPs possess Fenton-like activity, enabling them to catalyze the decomposition of H_2O_2 to produce ·OH, thereby significantly enhancing antibacterial efficiency. The experimental results indicated that the survival rates of *MRSA* and *PA* were further reduced when V_o-$AgFeO_{2-x}$ NPs were combined with a low concentration of H_2O_2 (Fig. 4(c) and Fig. S3 in the ESM). The statistical data further demonstrated that the antibacterial effect of the V_o-$AgFeO_{2-x}$ NPs was positively correlated with their concentration and that the antibacterial performance of the V_o-$AgFeO_{2-x}$ NPs was significantly enhanced when they were combined with H_2O_2 (Figs. 4(d) and 4(e)). In summary, the V_o-$AgFeO_{2-x}$ NPs exhibited excellent antibacterial properties. The mechanism of action involves not only the antibacterial characteristics of silver but also its synergistic effect with H_2O_2 to generate hydroxyl radicals, which substantially improves antibacterial efficiency. These results strongly support the potential applications of V_o-$AgFeO_{2-x}$ NPs in wound healing and other antibacterial applications.

To further analyze the antibacterial ability and mechanism of the V_o-$AgFeO_{2-x}$ NPs, the morphology and integrity of the bacteria under different conditions were observed via SEM. The untreated *MRSA* had a spherical morphology with a smooth surface, whereas the *PA* was usually straight or slightly curved with a blunt round rod at both ends. For *MRSA*, the surfaces of the cells in the control group and H_2O_2 group were smooth and complete, almost without damage, indicating that H_2O_2 itself had a limited influence on the integrity of the cell wall. In the V_o-$AgFeO_{2-x}$ NP group, the bacterial surface was slightly broken, irregular and uneven. However, when V_o-$AgFeO_{2-x}$ + H_2O_2 was used to treat the bacteria, the toxic ·OH produced by the V_o-$AgFeO_{2-x}$ NPs + H_2O_2 severely damaged the integrity of the bacteria, and the bacterial surface collapsed and shrunk (Fig. 4(g)). Similar phenomena were observed for *PA* under various treatments (Fig. 4(g)). The results showed that V_o-$AgFeO_{2-x}$ NPs combined with active oxygen can achieve the best antibacterial effect.

Moreover, a live/dead bacterial staining (N01/PI) assay was performed via confocal laser scanning microscopy (CLSM) to observe the antibacterial performance of the V_o-$AgFeO_{2-x}$ NPs after different treatments. Bacteria were stained with propidium iodide (PI, red fluorescence) and N01 (green fluorescence), which can be used to directly observe whether the bacteria are alive or dead (Figs. 5(a) and 5(b)). Consistent with previous results, the V_o-$AgFeO_{2-x}$ NPs effectively killed bacteria, but the effect was not ideal (Fig. S4 in the ESM). With the combined action of H_2O_2, they had better antibacterial properties.

3.4 *In vivo* antibacterial activity of the V_o-$AgFeO_{2-x}$ NPs

On the basis of the excellent antibacterial performance of the V_o-$AgFeO_{2-x}$ NPs observed *in vitro*, we further explored their application in wound healing in a mouse model (Fig. 6(a)). *MRSA* and *PA* are common pathogens in skin wound infections; thus, we established two skin wound infection models using *MRSA* and *PA*. Following successful infection, the BALB/c female mice were randomly divided into four groups: (I) the PBS control group, (II) the H_2O_2 treatment group, (III) the V_o-$AgFeO_{2-x}$ NP treatment group, and (IV) the V_o-$AgFeO_{2-x}$ NP + H_2O_2 combination treatment group. The results showed that wound healing was comparable between *MRSA* and *PA* infections. Both the control group and H_2O_2 treatment group exhibited slower wound healing, with a larger wound area remaining on day 11, indicating that H_2O_2 alone was insufficient to effectively promote wound healing. In contrast, compared with control and H_2O_2-treated mice, V_o-$AgFeO_{2-x}$ NP-treated mice presented progressive scab formation and a significantly faster wound healing rate, demonstrating that V_o-$AgFeO_{2-x}$ NPs effectively eradicated wound bacteria and accelerated healing. More notably, the combination treatment of V_o-$AgFeO_{2-x}$ NPs and H_2O_2 resulted in significantly superior wound healing compared with the other groups. On day 11 postinjection, the wounds in this group had nearly fully healed (Figs. 6(b) and 6(c)). Figure 6(d) shows the changes in wound size among the different groups on days 1, 3, 5, 7, 9, and 11. The percentage of the wound area was calculated to assess the healing rates (Figs. 6(d) and 6(e)). Compared with the other treatments, the V_o-$AgFeO_{2-x}$ NP + H_2O_2 combination treatment markedly improved wound healing. These findings suggest that the combination of V_o-$AgFeO_{2-x}$ NPs and H_2O_2 can effectively kill bacteria and significantly promote wound healing, providing an effective strategy for treating pathogenic microbial infections *in vivo*.

To further confirm this conclusion, we used hematoxylin and eosin (H&E) staining and Masson's trichrome staining for histological analysis. H&E staining is usually used to evaluate granulation tissue formation. H&E staining revealed that there were still more neutrophils in the infection site of the control group, while there were fewer neutrophils in the V_o-$AgFeO_{2-x}$ NPs + H_2O_2 group, and the epidermis was relatively complete (Figs. 7(a) and 7(b)). In addition, the quantitative measurement of the length of the histological wound sections in the four different treatment groups confirmed that the V_o-$AgFeO_{2-x}$ NPs + H_2O_2 had a better healing effect (Figs. 7(c) and 7(d)). Granulation tissue plays a critical role in the regenerative repair process of wounds accompanied by inflammation. Therefore, the thickness of granulation tissue is an important index for evaluating the extent of wound healing. In the *MRSA*-infected wounds, the thickness of the granulation tissue in the V_o-$AgFeO_{2-x}$ NPs + H_2O_2 group and the control group was not significantly different (Fig. S5 in the ESM). However, there was a significant difference between the two groups of *PA*-infected wounds, and the granulation tissue produced by the V_o-$AgFeO_{2-x}$ NPs + H_2O_2 group was thicker (Figs. 7(e) and 7(f)). Re-epithelization preceded the repair of the dermis and was considered to be the primary step during skin wound healing. It provides early functional barrier reconstruction for wounds to prevent excessive transdermal dehydration and wound infection. To confirm the re-epithelialization of the wounds and granulation tissue formation, we quantified the degree of epithelialization in each group of wounds. The degree of epithelialization in the V_o-$AgFeO_{2-x}$ NPs + H_2O_2 group was significantly greater than that in the control group, indicating that the V_o-$AgFeO_{2-x}$ NPs + H_2O_2 group exhibited the greatest extent of wound repair (Figs. 7(g) and 7(h)).

Collagen deposition and vascularization are also crucial for improving the formation of the extracellular matrix. Masson staining was used to verify the formation of collagen fibers during wound healing (blue represents collagen fibers). The density of collagen fibers in the V_o-$AgFeO_{2-x}$ NP + H_2O_2 group was the highest, indicating that the extent of wound repair was good (Figs. 8(a) and 8(b)). In conclusion, the prepared V_o-$AgFeO_{2-x}$ NPs improved the repair efficiency of infected wounds by promoting wound re-epithelialization and increasing collagen fiber deposition.

3.5 Biosafety of the V_o-$AgFeO_{2-x}$ NPs

Whether nanomaterials have reliable biological safety is an important factor that determines the application of nanomaterials

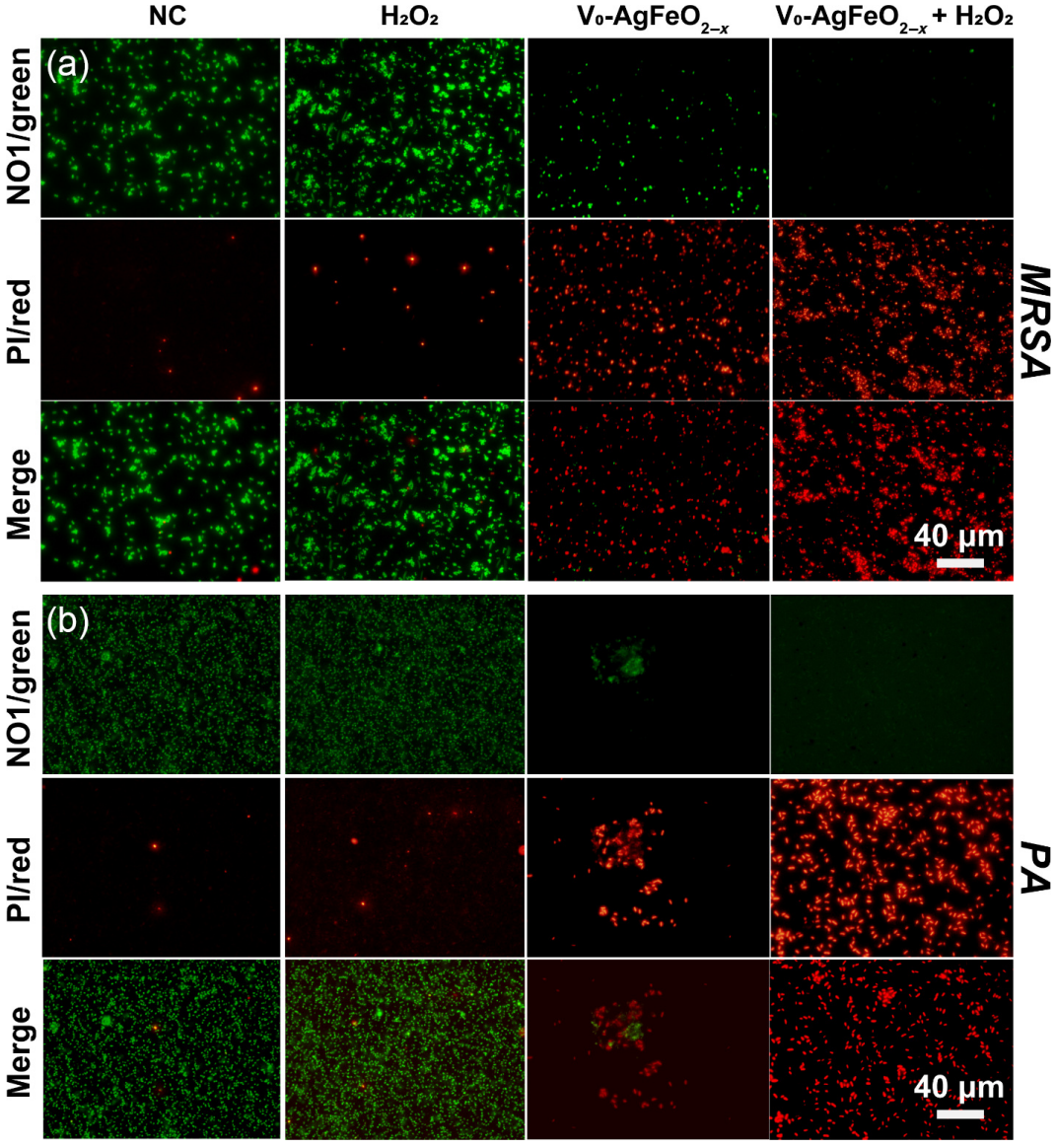

Figure 5 Live/dead staining of bacteria after different treatments. Live/dead fluorescence staining images of (a) *MRSA* and (b) *PA* using N01/PI after various therapies ($n = 3$).

in biomedicine. *In vitro* experiments with V_o-$AgFeO_{2-x}$ NPs at a high concentration of 500 μg/mL still revealed good cell survival (Fig. S6(a) in the ESM). In addition, the results of the hemolysis assay revealed that the V_o-$AgFeO_{2-x}$ NPs had excellent hemocompatibility (Fig. S6(b) in the ESM). During the entire experimental period, the mice grew well without any abnormalities, such as anorexia, weight loss or skin color changes. These findings indicated that the V_o-$AgFeO_{2-x}$ NPs had no significant toxicity to the mice. To further study whether V_o-$AgFeO_{2-x}$ NPs have toxicity and side effects *in vivo*, we collected blood samples and major organ tissues from mice in different treatment groups for testing and analysis. No obvious inflammation, abnormalities or damage was found by H&E staining of the main organs of the mice (Figs. 9(a) and 9(b)). Hematology analysis revealed that all blood parameters were within the normal range (Figs. 10(a) and 10(b)). These results indicate that the V_o-$AgFeO_{2-x}$ NPs have excellent biological safety *in vivo* and could be used as highly effective and safe wound antibacterial agents.

4 Conclusions

In summary, we designed and successfully prepared V_o-$AgFeO_{2-x}$ nanozymes and applied them to research the antibacterial activity of *MRSA* and *PA*. Owing to the presence of silver, the obtained V_o-$AgFeO_{2-x}$ nanozymes can denature bacterial proteins and increase permeability, thereby producing a greater killing effect on bacteria. In addition, the V_o-$AgFeO_{2-x}$ NPs exhibit excellent multienzyme activity and can react with H_2O_2 to produce reactive oxygen species, causing significant oxidative stress and damage to bacteria and further enhancing antibacterial efficacy. V_o-$AgFeO_{2-x}$ NPs can also scavenge free radicals, control inflammatory reactions, and accelerate wound healing. *In vitro* antibacterial experiments have shown that V_o-$AgFeO_{2-x}$ nanozymes can achieve satisfactory bactericidal effects in the presence of H_2O_2. *In vivo* experiments have shown that V_o-$AgFeO_{2-x}$ nanozymes can disinfect wounds infected with *MRSA* and *PA* and promote the deposition of collagen fibers and the formation of wound epithelium, thereby promoting wound healing. Moreover, the toxicity of the V_o-

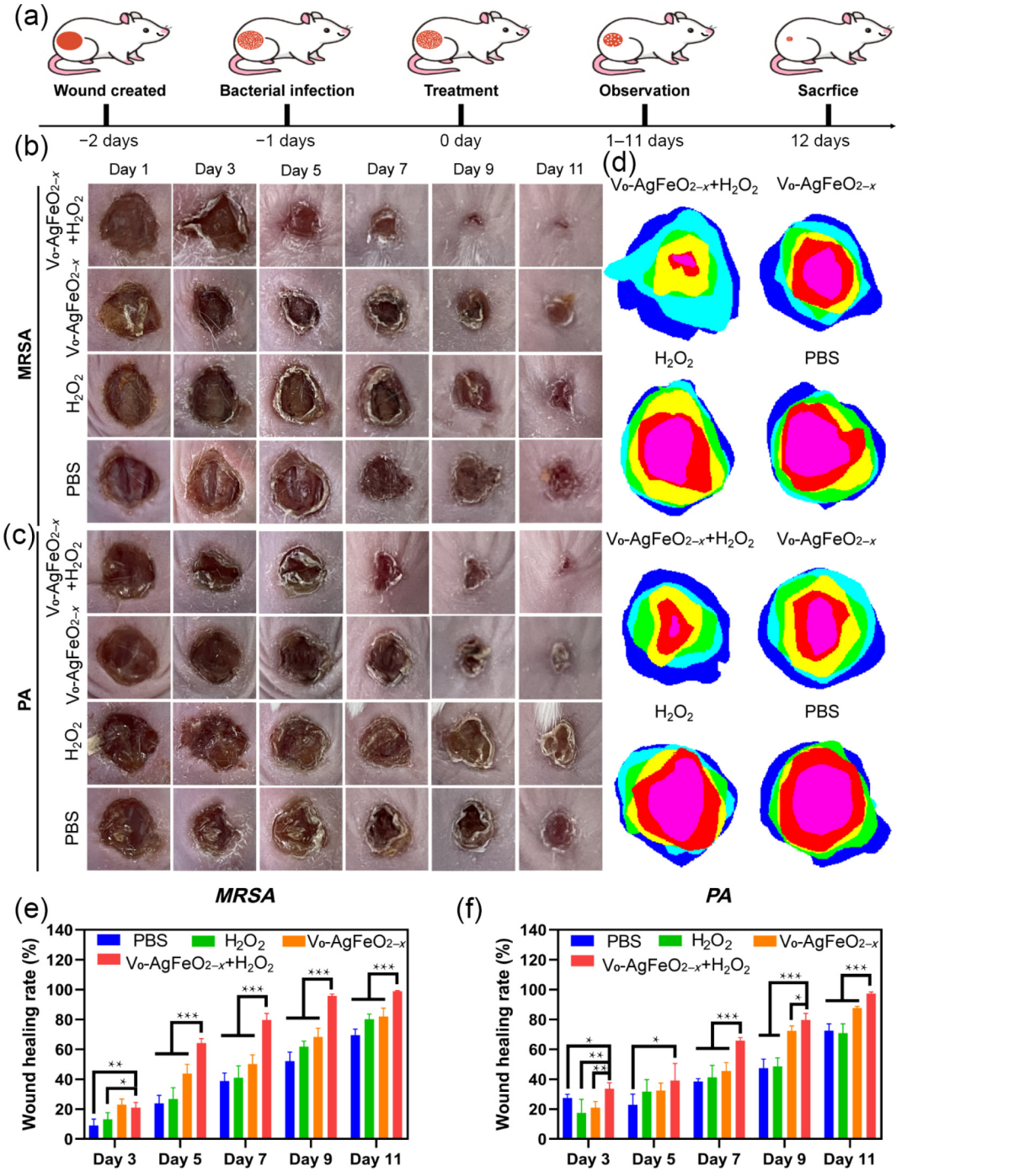

Figure 6 *In vivo* antibacterial performance of the V_o-$AgFeO_{2-x}$ NPs. (a) Schematic diagram of the wound infection model establishment and treatment process. (b) Photographs of *MRSA*-infected wounds and (e) wound healing rates of the mice after various treatments for 11 days. (c) Photographs of PA-infected wounds and (f) wound healing rates of the mice after various treatments for 11 days. (d) Schematic diagram of the wounds healed by different treatments for 11 days.

$AgFeO_{2-x}$ NPs to the animals was negligible, indicating that the V_o-$AgFeO_{2-x}$ NPs can be used as safe and effective wound disinfectants and antibacterial agents.

Electronic Supplementary Material: Supplementary material (enzyme activity of V_o-$AgFeO_{2-x}$ at different pH calues, the long-term stability of V_o-$AgFeO_{2-x}$ enzyme activity, relative bacterial viability of MRSA and PA after different treatments, statistics of the live (blue)/dead (red) fluorescence intensity, relative collagen content of MRSA and PA after different treatments, survival of different concentrations of V_o-$AgFeO_{2-x}$ in cells and hemolysis experiments) is available in the online version of this article at https://doi.org/10.26599/NR.2025.94907899.

Data availability

All data needed to support the conclusions in the paper are presented in the manuscript and the Electronic Supplementary Material. Additional data related to this paper may be requested from the corresponding author upon request.

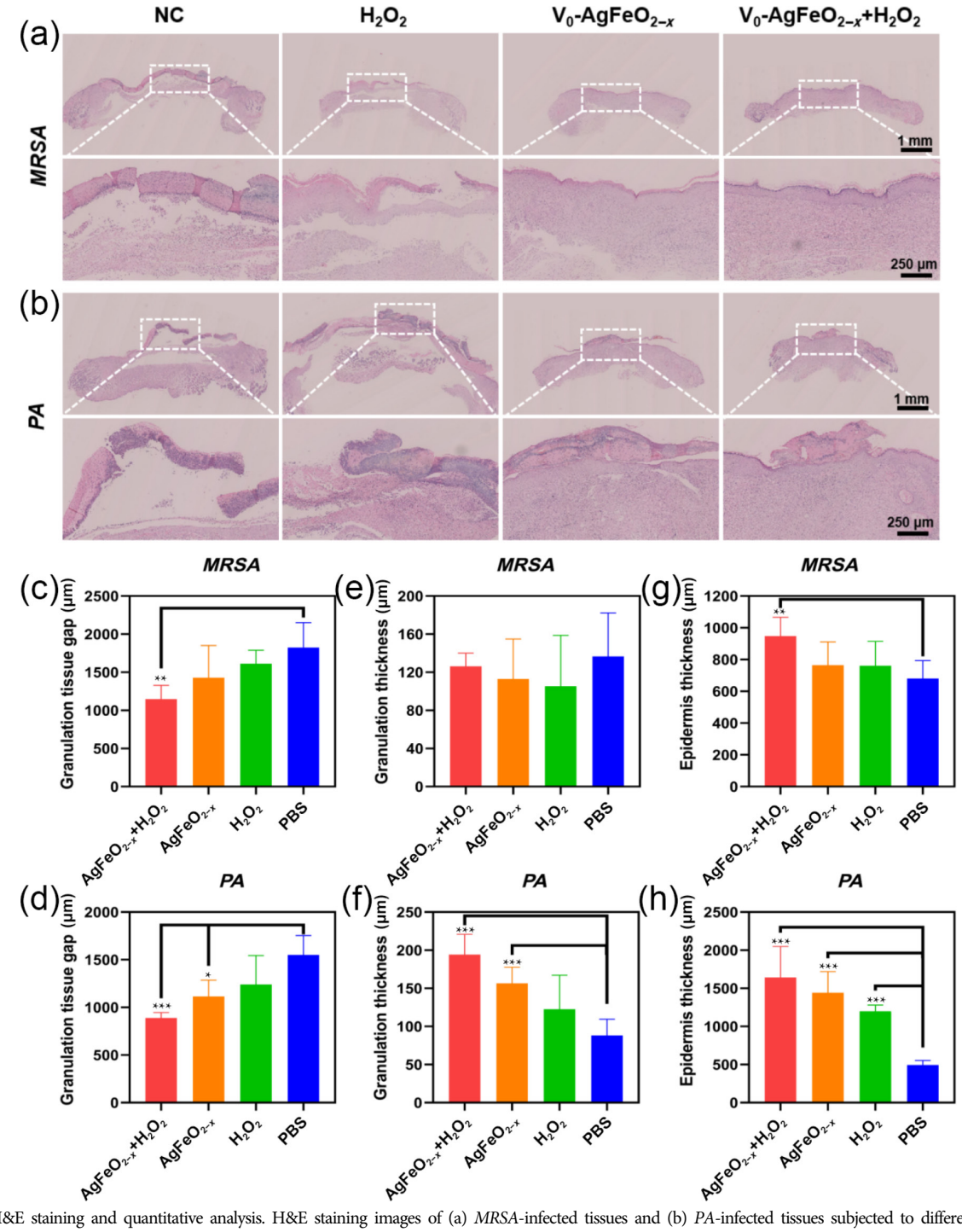

Figure 7 H&E staining and quantitative analysis. H&E staining images of (a) *MRSA*-infected tissues and (b) *PA*-infected tissues subjected to different treatments. Quantification of the cross-sectional length of (c) *MRSA*-infected wounds and (d) *PA*-infected wounds. Granulation tissue thickness of (e) *MRSA*-infected wounds and (f) *PA*-infected wounds. The epidermis thickness of (g) *MRSA*-infected wounds and (h) *PA*-infected wounds.

Acknowledgments

This work was supported by the Research Fund of the Anhui Institute of Translational Medicine (No. 2023zhyx-C51), the Youth Research Project of the Chinese Nursing Association (No. ZHKYQ202213), the Open Project of Engineering Research Center of Biofilm Water Purification and Utilization Technology of Ministry of Education (No. BWPU2020KF03), and the Natural Science Research Project of Anhui Higher Education Institution (No. 2023AH051127).

Declaration of competing interest

The authors declare that they have no competing financial interests.

Author contribution statement

H. R. C. and W. Q. W.: Data curation, project administration, validation, writing manuscript, experimental design. Y. J. L., L. S., F. N., H. C. M., and K. L. W.: Validation, data curation. T. X. Y. and L. S.: Supervision. X. W. W.: Project administration, funding

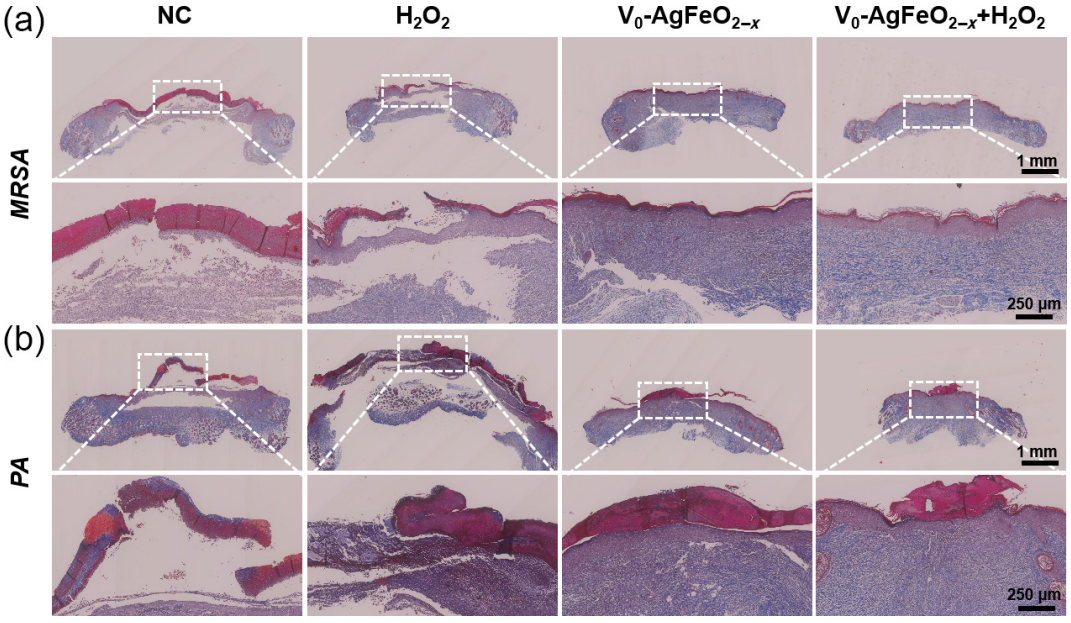

Figure 8 Masson staining. Masson staining images of (a) *MRSA*-infected tissues and (b) *PA*-infected tissues subjected to different treatments.

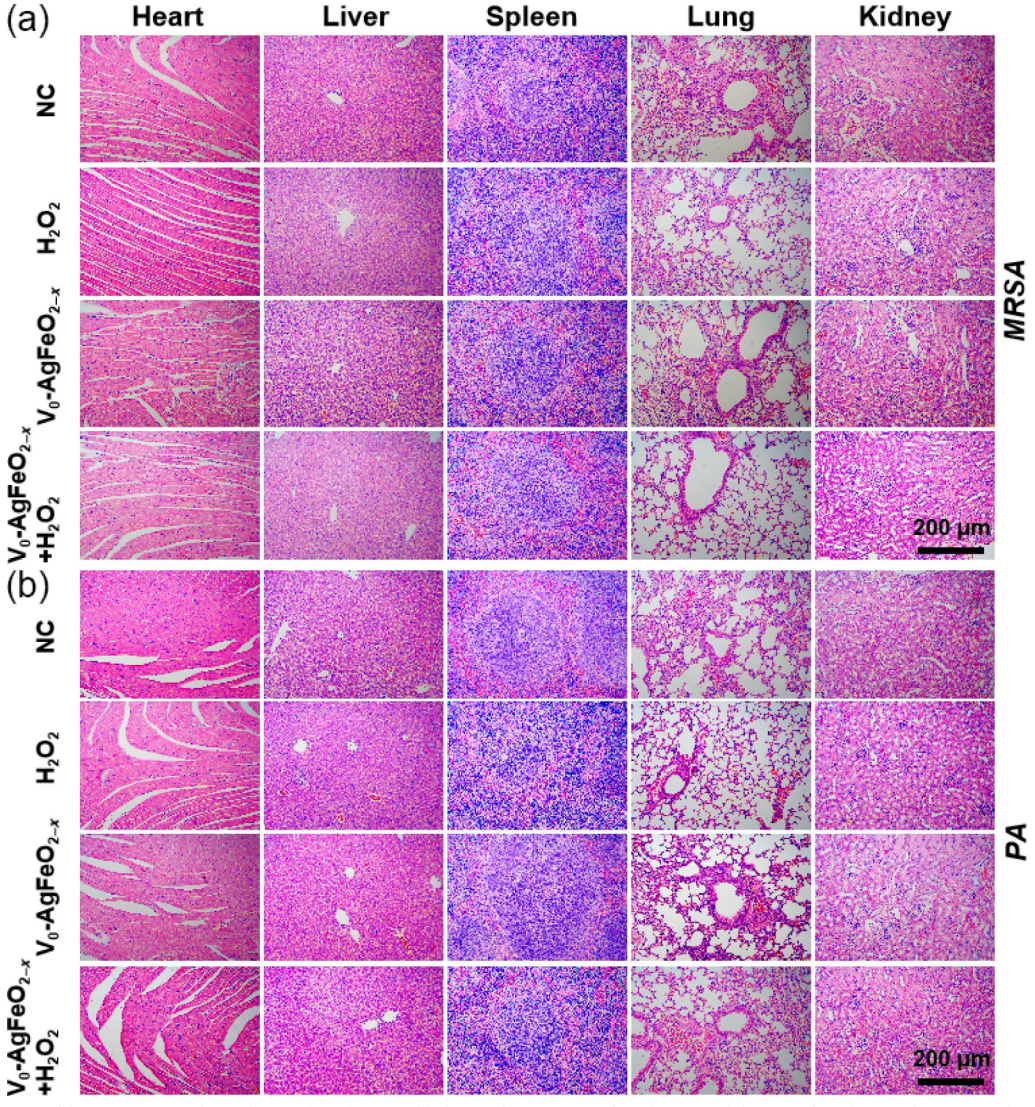

Figure 9 H&E staining of the main organs (heart, liver, spleen, lung, and kidney) of (a) *MRSA*-infected mice and (b) *PA*-infected mice after various therapies.

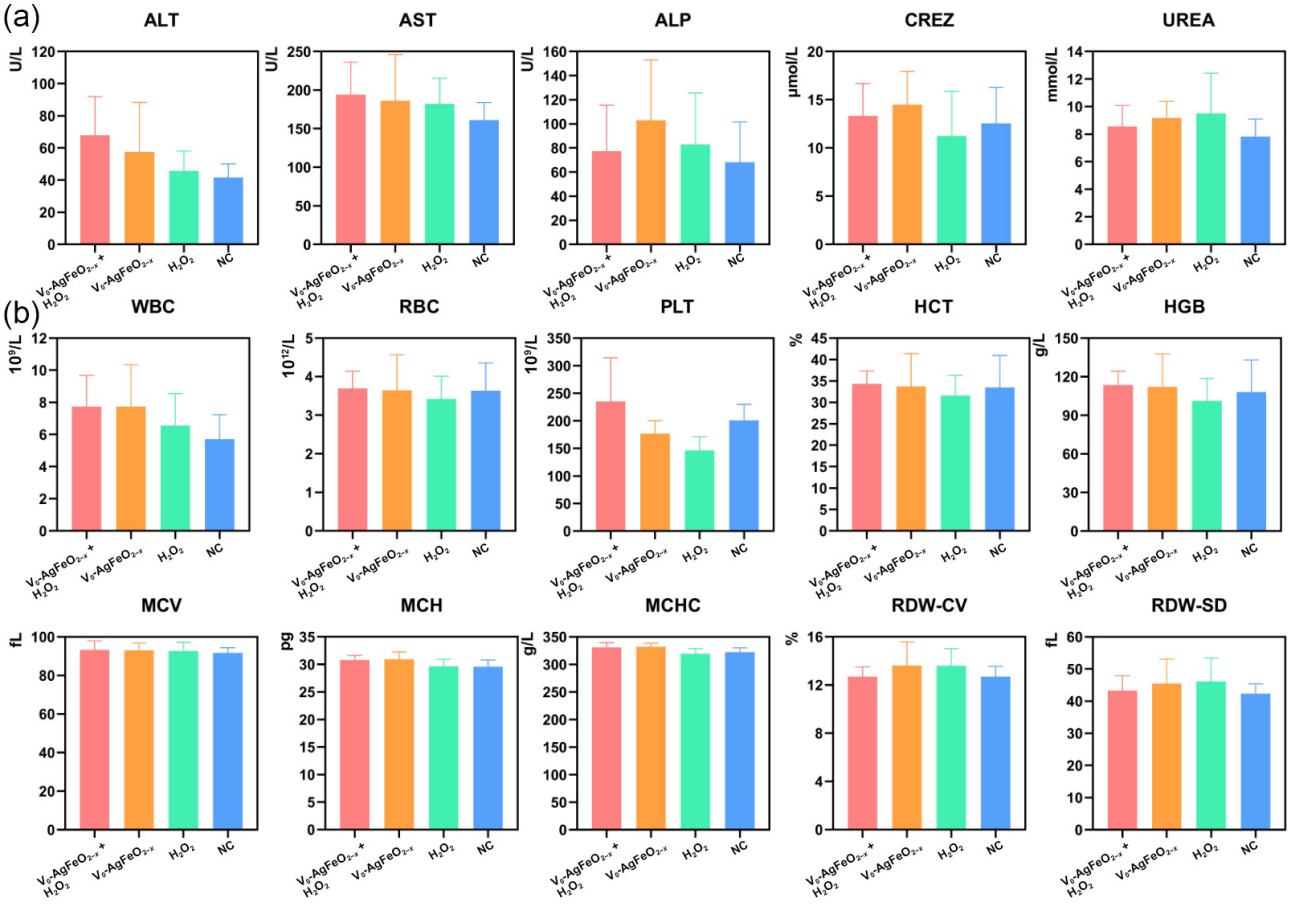

Figure 10 Hematology test. (a) Blood biochemistry and (b) routine blood tests of mice after various therapies.

acquisition, writing manuscript. All the authors have approved the final manuscript.

Informed consent

Not applicable.

Ethics statement

All animal procedures were performed in compliance with the guidelines of the Institutional Animal Care and Use Committee of the Department of Anhui Medical University (Ethical code: No. LLSC20220731).

Use of AI statement

None.

References

[1] Huang, K.; Liu, W. B.; Wei, W. Y.; Zhao, Y. N.; Zhuang, P. Z.; Wang, X. X.; Wang, Y. F.; Hu, Y. H.; Dai, H. L. Photothermal hydrogel encapsulating intelligently bacteria-capturing bio-MOF for infectious wound healing. *ACS Nano* **2022**, *16*, 19491–19508.

[2] Wells, A.; Nuschke, A.; Yates, C. C. Skin tissue repair: Matrix microenvironmental influences. *Matrix Biol.* **2016**, *49*, 25–36.

[3] Swoboda, L.; Held, J. Impaired wound healing in diabetes. *J. Wound Care* **2022**, *31*, 882–885.

[4] Wang, Z.; Qi, F.; Luo, H.; Xu, G. C.; Wang, D. L. Inflammatory microenvironment of skin wounds. *Front. Immunol.* **2022**, *13*, 789274.

[5] Deng, Y. T.; Gao, Y.; Li, T. T.; Xiao, S. T.; Adeli, M.; Rodriguez, R. D.; Geng, W.; Chen, Q.; Cheng, C.; Zhao, C. S. Amorphizing metal selenides-based ROS biocatalysts at surface nanolayer toward ultrafast inflammatory diabetic wound healing. *ACS Nano* **2023**, *17*, 2943–2957.

[6] Huang, C.; Dong, L. L.; Zhao, B. H.; Lu, Y. F.; Huang, S. R.; Yuan, Z. Q.; Luo, G. X.; Xu, Y.; Qian, W. Anti-inflammatory hydrogel dressings and skin wound healing. *Clin. Transl. Med.* **2022**, *12*, e1094.

[7] Zhang, Z. Y.; Zhang, Q.; Wang, T. Z.; Xu, N. H.; Lu, T.; Hong, W. J.; Penuelas, J.; Gillings, M.; Wang, M. X.; Gao, W. W. et al. Assessment of global health risk of antibiotic resistance genes. *Nat. Commun.* **2022**, *13*, 1553.

[8] Zhao, P.; Zhang, Y.; Chen, X. A.; Xu, C.; Guo, J. Z.; Deng, M. G.; Qu, X. W.; Huang, P. S.; Feng, Z. J.; Zhang, J. M. Versatile hydrogel dressing with skin adaptiveness and mild photothermal antibacterial activity for methicillin-resistant staphylococcus aureus-infected dynamic wound healing. *Adv. Sci.* **2023**, *10*, 2206585.

[9] Wang, W. Q.; Cui, Y. Y.; Wei, X. L.; Zang, Y.; Chen, X. L.; Cheng, L.; Wang, X. W. $CuCo_2O_4$ nanoflowers with multiple enzyme activities for treating bacterium-infected wounds via cuproptosis-like death. *ACS Nano* **2024**, *18*, 15845–15863.

[10] Jia, Q. Y.; Song, Q.; Li, P.; Huang, W. Rejuvenated photodynamic therapy for bacterial infections. *Adv. Healthcare Mater.* **2019**, *8*, 1900608.

[11] Liang, M. M.; Shang, L. M.; Yu, Y. X.; Jiang, Y. J.; Bai, Q.; Ma, J. C.; Yang, D. Q.; Sui, N.; Zhu, Z. L. Ultrasound activatable microneedles for bilaterally augmented sono-chemodynamic and sonothermal antibacterial therapy. *Acta Biomater.* **2023**, *158*, 811–826.

[12] Padre, S. M.; Kiruthika, S.; Mundinamani, S.; Ravikirana, Surabhi, S.; Jeong, J. R.; Eshwarappa, K. M.; Murari, M. S.; Shetty, V.; Ballal, M. et al. Mono- and bimetallic nanoparticles for catalytic degradation of hazardous organic dyes and antibacterial applications. *ACS Omega* **2022**, *7*, 35023–35034.

[13] Gao, F.; Shao, T. Y.; Yu, Y. P.; Xiong, Y. J.; Yang, L. H. Surface-bound reactive oxygen species generating nanozymes for selective antibacterial action. *Nat. Commun.* **2021**, *12*, 745.

[14] Yang, X. T.; Yu, Q. J.; Gao, W.; Tang, X. N.; Yi, H. H.; Tang, X. L. The mechanism of metal-based antibacterial materials and the progress of food packaging applications: A review. *Ceram. Int.* **2022**, *48*, 34148–34168.

[15] Wang, W. Q.; Gui, H. S.; Wei, X. L.; Liu, H. Y.; Wang, X. W. Cuproptosis to cuproptosis-like: Therapeutic strategies for bacterial infection. *Adv. Mater.*, in press, https://doi.org/10.1002/adma.202506119.

[16] Hashem, A. H.; Al-Askar, A. A.; Saeb, M. R.; Abd-Elsalam, K. A.; El-Hawary, A. S.; Hasanin, M. S. Sustainable biosynthesized bimetallic ZnO@SeO nanoparticles from pomegranate peel extracts: Antibacterial, antifungal and anticancer activities. *RSC Adv.* **2023**, *13*, 22918–22927.

[17] Wang, W. Q.; Gao, P.; Gui, H. S.; Wei, X. L.; Zhang, H. G.; Wang, X. W. Copper-based nanomaterials for the treatment of bacteria-infected wounds: Material classification, strategies and mechanisms. *Coord. Chem. Rev.* **2025**, *522*, 216205.

[18] Pelgrift, R. Y.; Friedman, A. J. Nanotechnology as a therapeutic tool to combat microbial resistance. *Adv. Drug Delivery Rev.* **2013**, *65*, 1803–1815.

[19] Dizaj, S. M.; Lotfipour, F.; Barzegar-Jalali, M.; Zarrintan, M. H.; Adibkia, K. Antimicrobial activity of the metals and metal oxide nanoparticles. *Mater. Sci. Eng.: C* **2014**, *44*, 278–284.

[20] Bytešníková, Z.; Pečenka, J.; Tekielska, D.; Kiss, T.; Švec, P.; Ridošková, A.; Bezdička, P.; Pekárková, J.; Eichmeier, A.; Pokluda, R. et al. Reduced graphene oxide-based nanometal-composite containing copper and silver nanoparticles protect tomato and pepper against *Xanthomonas euvesicatoria* infection. *Chem. Biol. Technol. Agric.* **2022**, *9*, 84.

[21] Charkhabi, S.; Jackson, K. J.; Beierle, A. M.; Carr, A. R.; Zellner, E. M.; Reuel, N. F. Monitoring wound health through bandages with passive LC resonant sensors. *ACS Sens.* **2021**, *6*, 111–122.

[22] Cheng, X. Q.; Zhang, S.; Liu, H. H.; Chen, H. M.; Zhou, J. H.; Chen, Z. W.; Zhou, X.; Xie, Z. X.; Kuang, Q.; Zheng, L. S. Biomimetic metal-organic framework composite-mediated cascade catalysis for synergistic bacteria killing. *ACS Appl. Mater. Interfaces* **2020**, *12*, 36996–37005.

[23] Alavi, M.; Li, L.; Nokhodchi, A. Metal, metal oxide and polymeric nanoformulations for the inhibition of bacterial quorum sensing. *Drug Discovery Today* **2023**, *28*, 103392.

[24] Barrientos, S.; Stojadinovic, O.; Golinko, M. S.; Brem, H.; Tomic-Canic, M. PERSPECTIVE ARTICLE: Growth factors and cytokines in wound healing. *Wound Repair Regener.* **2008**, *16*, 585–601.

[25] Chao, D. Y.; Dong, Q.; Chen, J. X.; Yu, Z. X.; Wu, W. W.; Fang, Y. X.; Liu, L.; Dong, S. J. Highly efficient disinfection based on multiple enzyme-like activities of Cu_3P nanoparticles: A catalytic approach to impede antibiotic resistance. *Appl. Catal. B: Environ.* **2022**, *304*, 121017.

[26] Ge, J.; Li, M. T.; Fan, J. H.; Celia, C.; Xie, Y. J.; Chang, Q.; Deng, X. Y. Synthesis, characterization, and antibacterial activity of chitosan-chelated silver nanoparticles. *J. Biomater. Sci. Polym. Ed.* **2024**, *35*, 45–62.

[27] Almutairi, H. H.; Parveen, N.; Ansari, S. A. Hydrothermal synthesis of multifunctional bimetallic Ag-CuO nanohybrids and their antimicrobial, antibiofilm and antiproliferative potential. *Nanomaterials* **2022**, *12*, 4167.

[28] Islam, R.; Bilal, H.; Wang, X. J.; Zhang, L. B. Tripeptides ghk and GhkCu-modified silver nanoparticles for enhanced antibacterial and wound healing activities. *Colloids Surf. B: Biointerfaces* **2024**, *236*, 113785.

[29] Lu, Z. Y.; Yu, D.; Nie, F. S.; Wang, Y.; Chong, Y. Iron nanoparticles open up new directions for promoting healing in chronic wounds in the context of bacterial infection. *Pharmaceutics* **2023**, *15*, 2327.

[30] Bhattacharjee, R.; Kumar, L.; Mukerjee, N.; Anand, U.; Dhasmana, A.; Preetam, S.; Bhaumik, S.; Sihi, S.; Pal, S.; Khare, T. et al. The emergence of metal oxide nanoparticles (NPs) as a phytomedicine: A two-facet role in plant growth, nano-toxicity and anti-phyto-microbial activity. *Biomed. Pharmacother.* **2022**, *155*, 113658.

[31] Hashemi, Z.; Ebrahimzadeh, M. A.; Biparva, P.; Mortazavi-Derazkola, S.; Goli, H. R.; Sadeghian, F.; Kardan, M.; Rafiei, A. Biogenic silver and zero-valent iron nanoparticles by feijoa: Biosynthesis, characterization, cytotoxic, antibacterial and antioxidant activities. *Anti-Cancer Agents Med. Chem.* **2020**, *20*, 1673–1687.

[32] Saqib, S.; Munis, M. F. H.; Zaman, W.; Ullah, F.; Shah, S. N.; Ayaz, A.; Farooq, M.; Bahadur, S. Synthesis, characterization and use of iron oxide nano particles for antibacterial activity. *Microsc. Res. Tech.* **2019**, *82*, 415–420.

[33] Shehata, A. M.; Salem, F. M. S.; El-Saied, E. M.; Abd El-Rahman, S. S.; Mahmoud, M. Y.; Noshy, P. A. Evaluation of the ameliorative effect of zinc nanoparticles against silver nanoparticle-induced toxicity in liver and kidney of rats. *Biol. Trace Elem. Res.* **2022**, *200*, 1201–1211.

[34] Anbouhi, T. S.; Esfidvajani, E. M.; Nemati, F.; Haghighat, S.; Sari, S.; Attar, F.; Pakaghideh, A.; Sohrabi, M. J.; Mousavi, S. E.; Falahati, M. Albumin binding, anticancer and antibacterial properties of synthesized zero valent iron nanoparticles. *Int. J. Nanomedicine* **2018**, *14*, 243–256.

[35] Alavi, M.; Karimi, N. Characterization, antibacterial, total antioxidant, scavenging, reducing power and ion chelating activities of green synthesized silver, copper and titanium dioxide nanoparticles using *Artemisia haussknechtii* leaf extract. *Artif. Cells Nanomed. Biotechnol.* **2018**, *46*, 2066–2081.

[36] Malik, M. A.; Albeladi, S. S. R.; Al-Maaqar, S. M.; Alshehri, A. A.; Al-Thabaiti, S. A.; Khan, I.; Kamli, M. R. Biosynthesis of novel Ag-Cu bimetallic nanoparticles from leaf extract of *Salvia officinalis* and their antibacterial activity. *Life* **2023**, *13*, 653.

[37] Padilla-Cruz, A. L.; Garza-Cervantes, J. A.; Vasto-Anzaldo, X. G.; García-Rivas, G.; León-Buitimea, A.; Morones-Ramírez, J. R. Synthesis and design of Ag-Fe bimetallic nanoparticles as antimicrobial synergistic combination therapies against clinically relevant pathogens. *Sci. Rep.* **2021**, *11*, 5351.

[38] Fu, R. X.; Ma, Z. J.; Zhao, H. B.; Jin, H.; Tang, Y.; He, T.; Ding, Y. P.; Zhang, J. J.; Ye, D. X. Research progress in iron-based nanozymes: Catalytic mechanisms, classification, and biomedical applications. *Anal. Chem.* **2023**, *95*, 10844–10858.

[39] Wright, J. A.; Richards, T.; Srai, S. K. S. The role of iron in the skin and cutaneous wound healing. *Front. Pharmacol.* **2014**, *5*, 156.

[40] Liu, G. Y.; Zhu, J. W.; Guo, H.; Sun, A. H.; Chen, P.; Xi, L.; Huang, W.; Song, X. J.; Dong, X. C. Mo_2C-derived polyoxometalate for NIR–II photoacoustic imaging-guided chemodynamic/photothermal synergistic therapy. *Angew. Chem., Int. Ed.* **2019**, *58*, 18641–18646.

[41] Verdolino, D. V.; Thomason, H. A.; Fotticchia, A.; Cartmell, S. Wound dressings: Curbing inflammation in chronic wound healing. *Emerg. Top. Life Sci.* **2021**, *5*, 523–537.

[42] Baron, J. M.; Glatz, M.; Proksch, E. Optimal support of wound healing: New insights. *Dermatology* **2020**, *236*, 593–600.

[43] Liang, Y. P.; Li, M.; Yang, Y. T.; Qiao, L. P.; Xu, H. R.; Guo, B. L.

pH/glucose dual responsive metformin release hydrogel dressings with adhesion and self-healing via dual-dynamic bonding for athletic diabetic foot wound healing. *ACS Nano* **2022**, *16*, 3194–3207.

[44] Wołosiak, R.; Drużyńska, B.; Derewiaka, D.; Piecyk, M.; Majewska, E.; Ciecierska, M.; Worobiej, E.; Pakosz, P. Verification of the conditions for determination of antioxidant activity by ABTS and DPPH assays-a practical approach. *Molecules* **2022**, *27*, 50.

[45] Niu, B. Y.; Liao, K. X.; Zhou, Y. X.; Wen, T.; Quan, G. L.; Pan, X.; Wu, C. B. Application of glutathione depletion in cancer therapy: Enhanced ROS-based therapy, ferroptosis, and chemotherapy. *Biomaterials* **2021**, *277*, 121110.

[46] Liu, G.; Liu, M. Y.; Li, X. J.; Ye, X. R.; Cao, K. M.; Liu, Y. Z.; Yu, Y. Peroxide-simulating and GSH-depleting nanozyme for enhanced chemodynamic/photodynamic therapy via induction of multisource ROS. *ACS Appl. Mater. Interfaces* **2023**, *15*, 47955–47968.

[47] Li, L.; Liu, H.; Bian, J. X.; Zhang, X. Y.; Fu, Y. H.; Li, Z.; Wei, S. P.; Xu, Z. C.; Liu, X. K.; Liu, Z. W. et al. Ag/Pd bimetal nanozyme with enhanced catalytic and photothermal effects for ROS/hyperthermia/chemotherapy triple-modality antitumor therapy. *Chem. Eng. J.* **2020**, *397*, 125438.

[48] Li, S. Q.; Hou, Y. J.; Chen, Q. M.; Zhang, X. D.; Cao, H. Y.; Huang, Y. M. Promoting active sites in MOF-derived homobimetallic hollow nanocages as a high-performance multifunctional nanozyme catalyst for biosensing and organic pollutant degradation. *ACS Appl. Mater. Interfaces* **2020**, *12*, 2581–2590.

[49] Sun, M. M.; He, M. X.; Jiang, S. J.; Wang, Y. Y.; Wang, X. X.; Liu, T.; Song, C.; Wang, S. N.; Rao, H. B.; Lu, Z. W. Multi-enzyme activity of three layers FeO_x@ZnMnFeO_y@Fe-Mn organogel for colorimetric detection of antioxidants and norfloxacin with smartphone. *Chem. Eng. J.* **2021**, *425*, 131823.

[50] Ivanova, M. N.; Grayfer, E. D.; Plotnikova, E. E.; Kibis, L. S.; Darabdhara, G.; Boruah, P. K.; Das, M. R.; Fedorov, V. E. Pt-decorated boron nitride nanosheets as artificial nanozyme for detection of dopamine. *ACS Appl. Mater. Interfaces* **2019**, *11*, 22102–22112.

[51] Duan, W.; Qiu, Z. W.; Cao, S. F.; Guo, Q.; Huang, J. K.; Xing, J. Y.; Lu, X. Q.; Zeng, J. B. Pd-Fe_3O_4 Janus nanozyme with rational design for ultrasensitive colorimetric detection of biothiols. *Biosens. Bioelectronics* **2022**, *196*, 113724.

[52] Gong, F.; Yang, N. L.; Wang, Y.; Zhuo, M. P.; Zhao, Q.; Wang, S.; Li, Y. G.; Liu, Z.; Chen, Q.; Cheng, L. Oxygen-deficient bimetallic oxide $FeWO_X$ nanosheets as peroxidase-like nanozyme for sensing cancer via photoacoustic imaging. *Small* **2020**, *16*, 2003496.

[53] Shi, Z. J.; Wang, T.; Lin, H. Y.; Wang, X. H.; Ding, J. J.; Shao, M. W. Excellent surface-enhanced Raman scattering (SERS) based on $AgFeO_2$ semiconductor nanoparticles. *Nanoscale* **2013**, *5*, 10029–10033.